Supporting Information

Ionic liquid-hydroxide-mediated Low-temperature Synthesis of High-entropy Perovskite Oxides Nanoparticles

Yingying Shi[a], Qiuchen Xu[a], Zhangmin Tian[a], Guiying Liu[a], Chenxu Ma[a]

and Wenjun Zheng*[,a,b]

a. Department of Chemistry, Key Laboratory of Advanced Energy Materials Chemistry (MOE), TKL of Metal and Molecule-based Material Chemistry, College of Chemistry, Nankai University, Tianjin, 300071, P. R. China.

b. Collaborative Innovation Center of Chemical Science and Engineering, Nankai University, Tianjin, 300071, P. R. China.

*Corresponding author. Tel.: +86 22 23507951. Fax: +86 22 23502458. E-mail: zhwj@nankai.edu.cn.
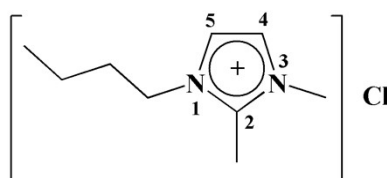
Fig. S1. Structure of [BMMIm]Cl (1-butyl-2,3-dimethylimidazolium chloride).
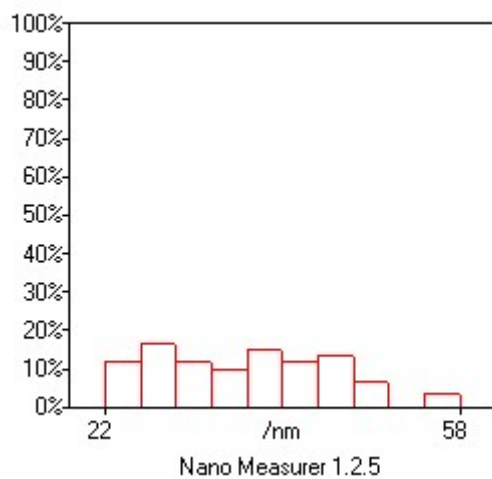
Fig. S2. The size distribution counting of Ba(FeNbTiZrTa)O_3 in Fig. 3a.
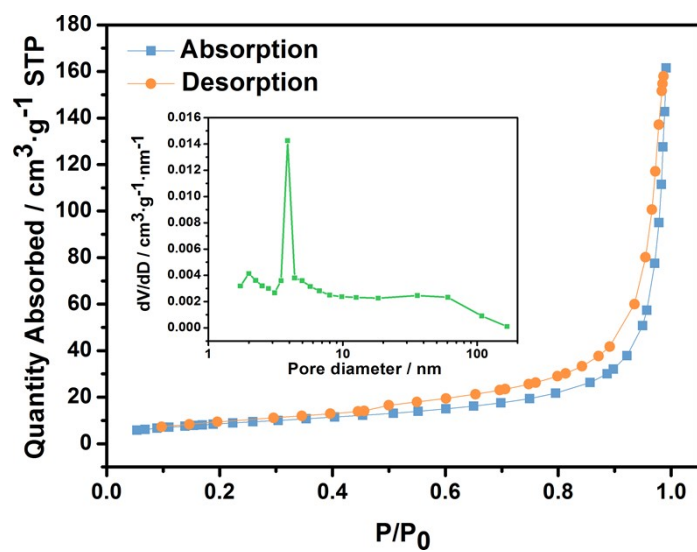
Fig. S3. N_2 adsorption-desorption isotherm and pore size distribution of Ba(FeNbTiZrTa)O_3.
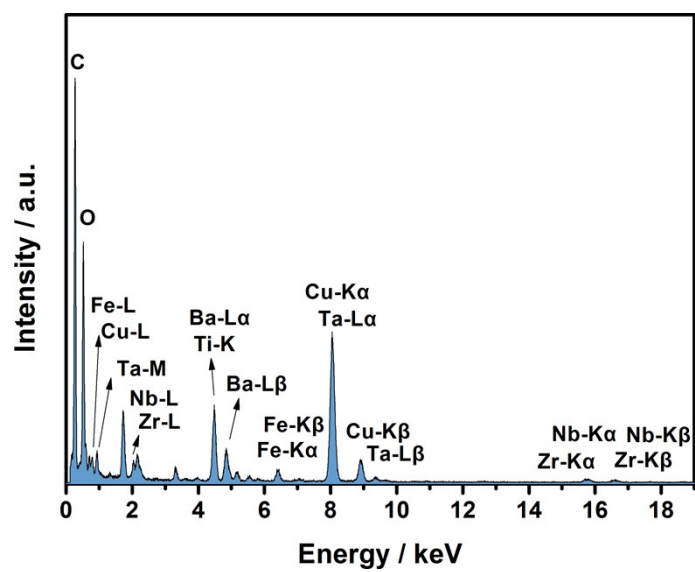
Fig. S4. EDX spectrum of Ba(FeNbTiZrTa)O$_3$.
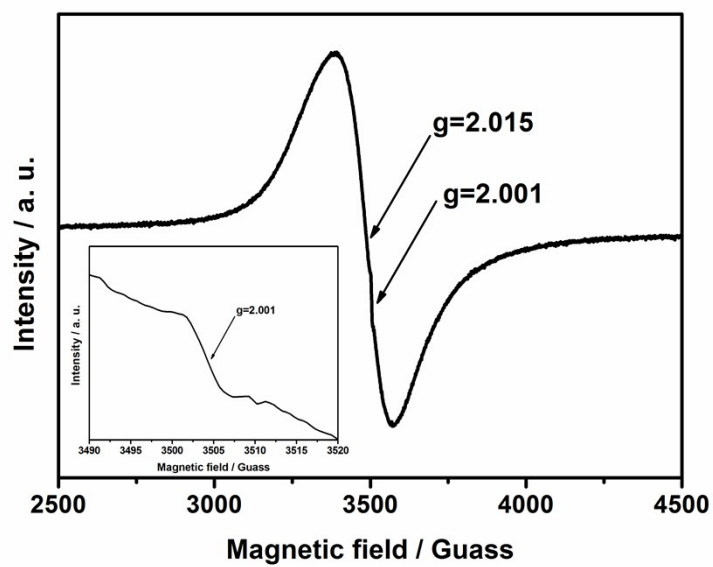
Fig. S5. Room temperature EPR spectrum of Ba(FeNbTiZrTa)O$_3$.
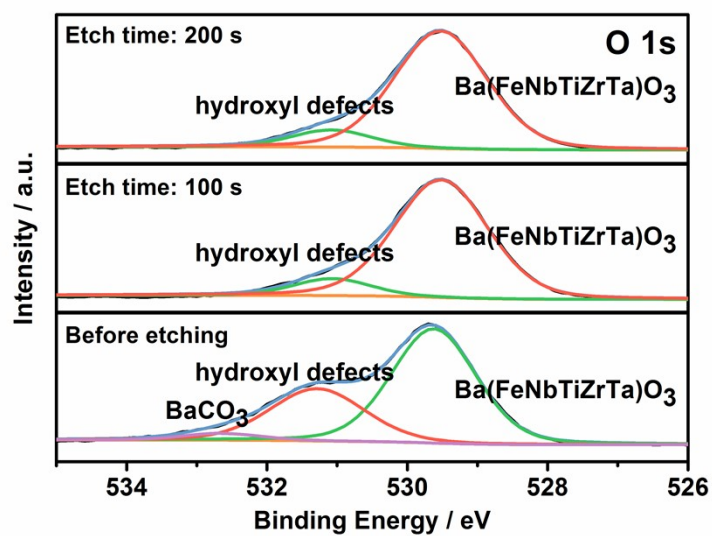
Fig. S6. The depth profiled XPS spectra of O 1s in Ba(FeNbTiZrTa)O$_3$.
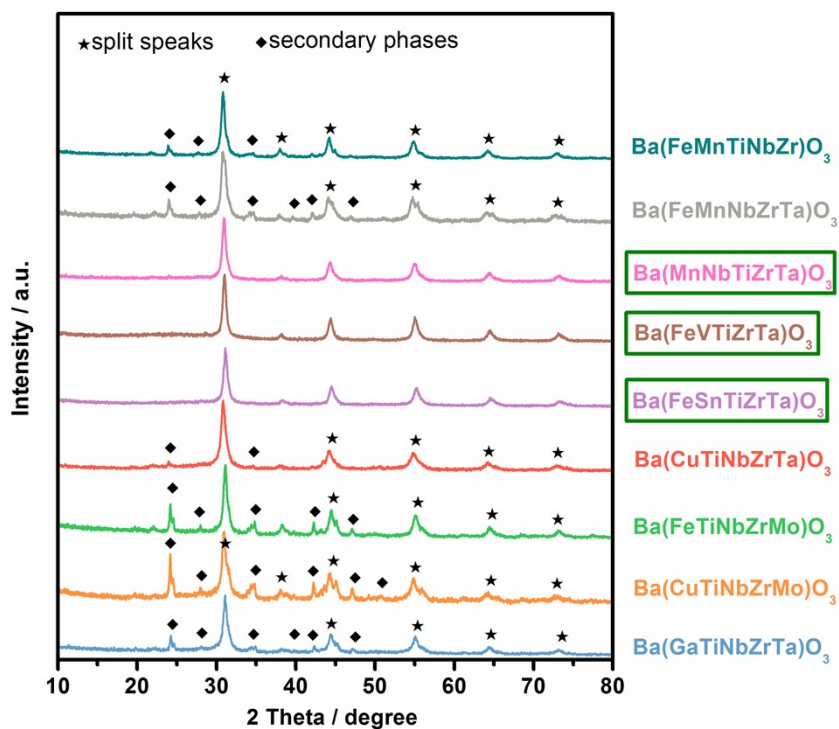
Fig. S7. XRD patterns for ABO$_3$ with five metals at B site, in which single-phase HEPOs are marked with green frames. The raw cation-supplying materials of Cu, Mo and Ga sources are Cu(NO$_3$)$_2$·3H$_2$O, MoO$_3$ and Ga(NO$_3$)$_3$·H$_2$O, respectively.
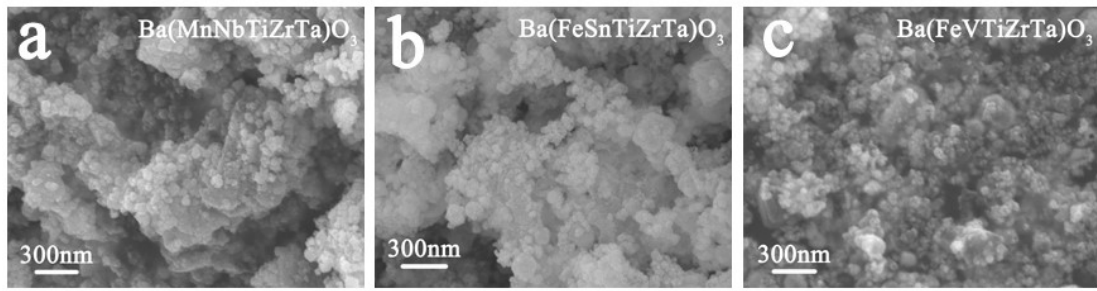
Fig. S8. SEM images of (a) Ba(MnNbTiZrTa)O$_3$, (b) Ba(FeSnTiZrTa)O$_3$ and (c) Ba(FeVTiZrTa)O$_3$.
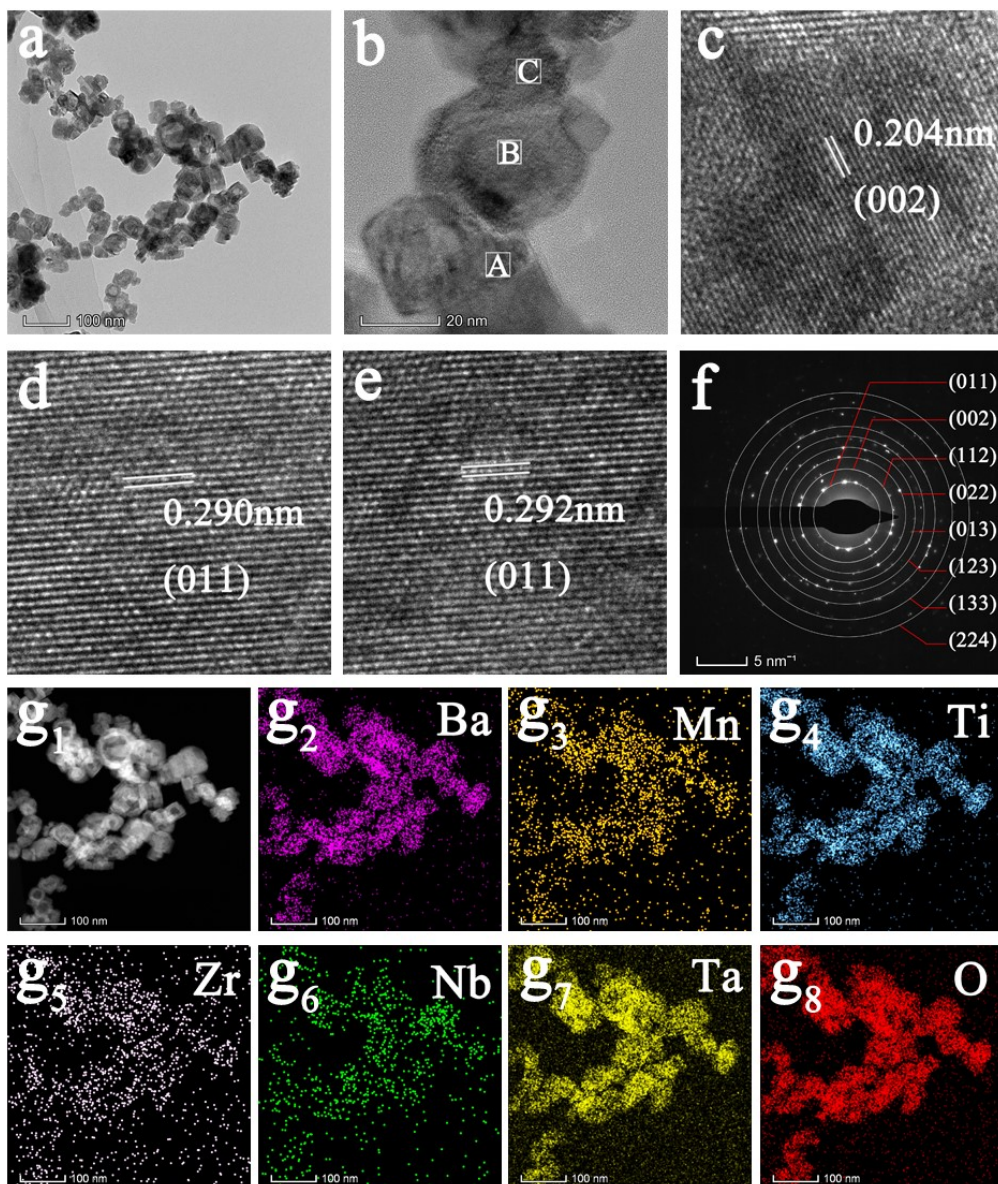
Fig. S9. (a) TEM image, (b-e) HRTEM images (Fig. S9c, Fig. S9d and Fig. S9e are the micrographs of region A, B and C in Fig. S9b, respectively), (f) corresponding SAED pattern and (g) EDX elemental mappings of Ba(MnNbTiZrTa)O$_3$.
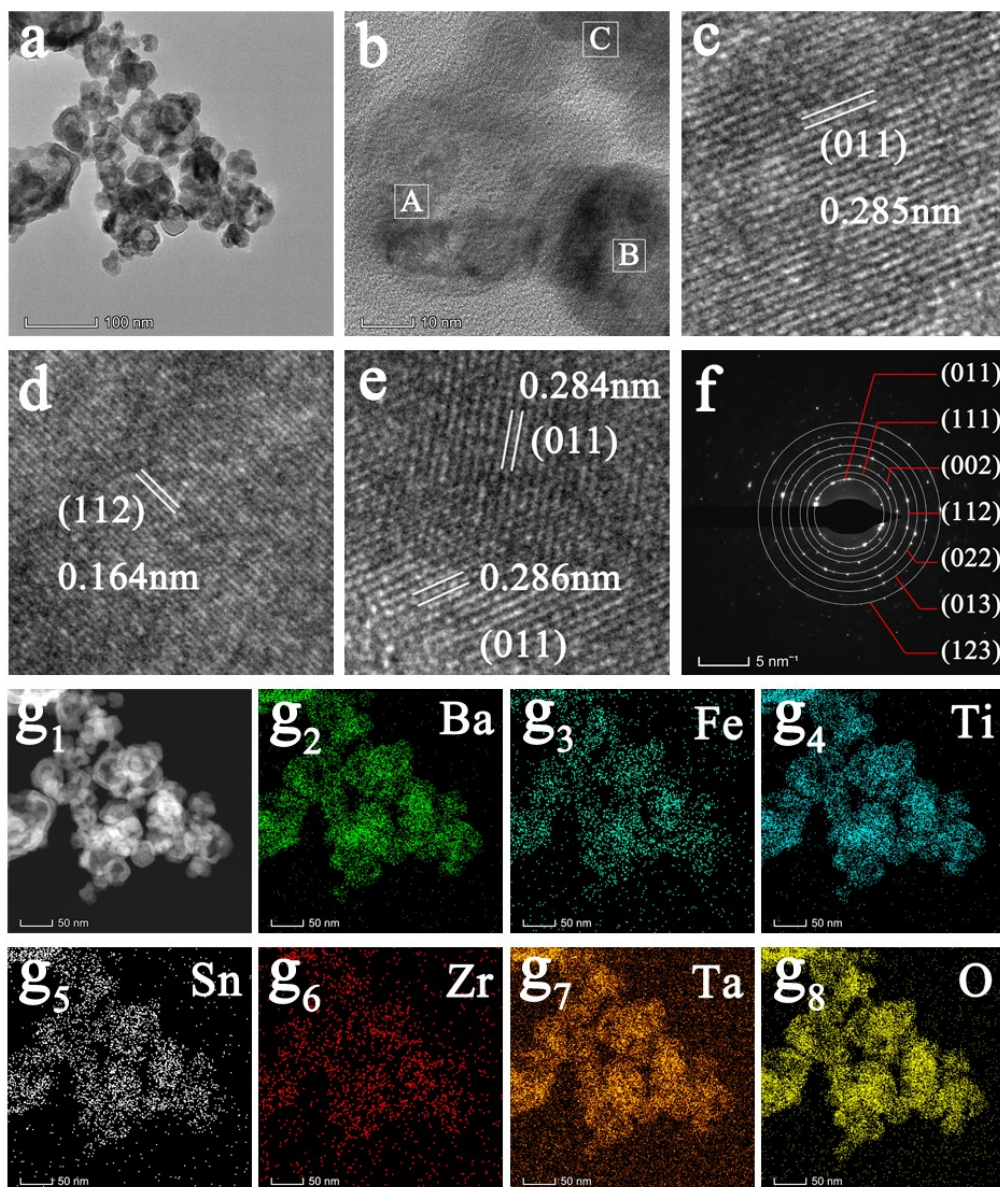
Fig. S10. (a) TEM image, (b-e) HRTEM images (Fig. S10c, Fig. S10d and Fig. S10e are the micrographs of region A, B and C in Fig. S10b, respectively), (f) corresponding SAED pattern and (g) EDX elemental mappings of Ba(FeSnTiZrTa)O$_3$.
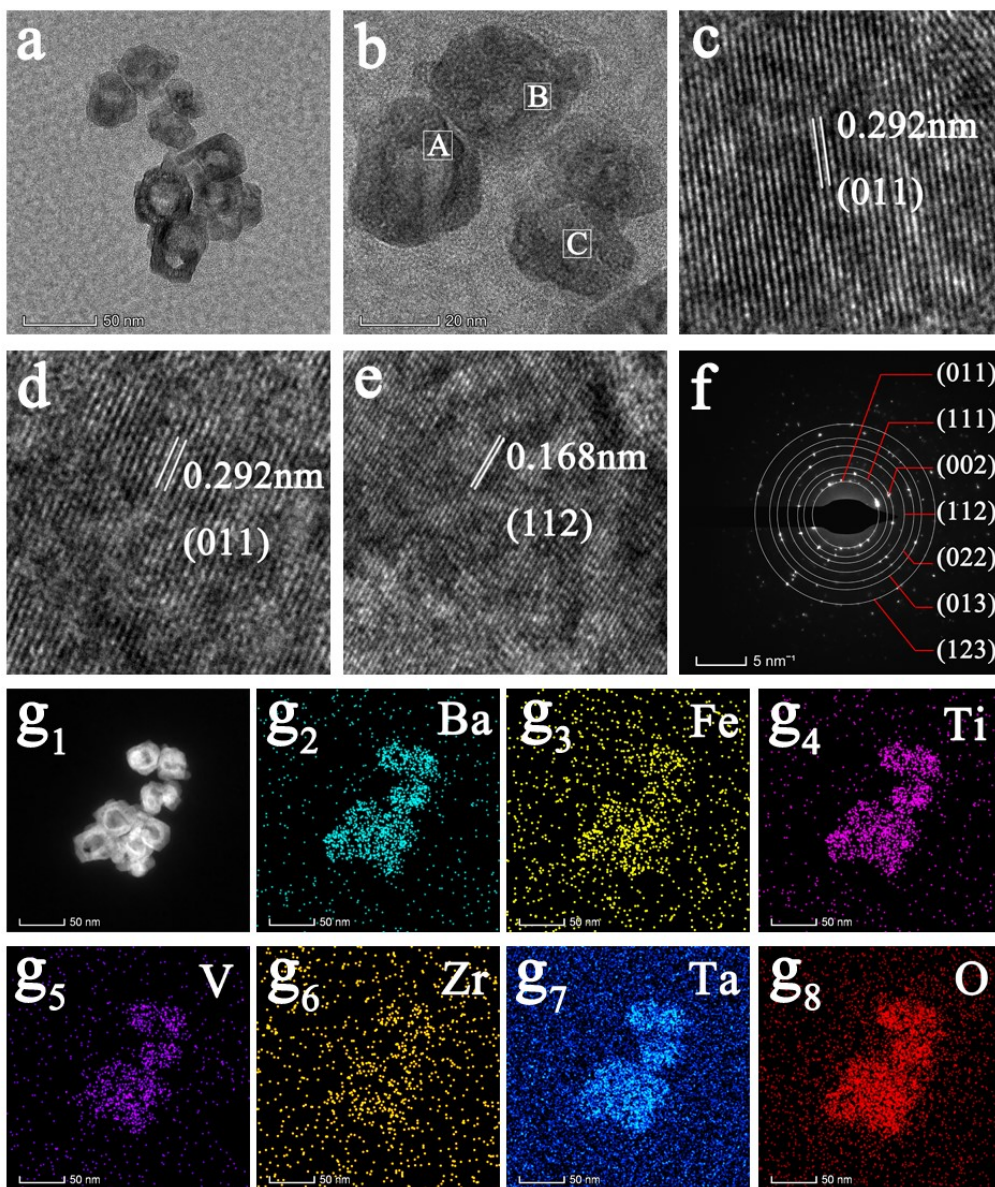
Fig. S11. (a) TEM image, (b-e) HRTEM images (Fig. S11c, Fig. S11d and Fig. S11e are the micrographs of region A, B and C in Fig. S11b, respectively), (f) corresponding SAED pattern and (g) EDX elemental mappings of Ba(FeVTiZrTa)O$_3$.
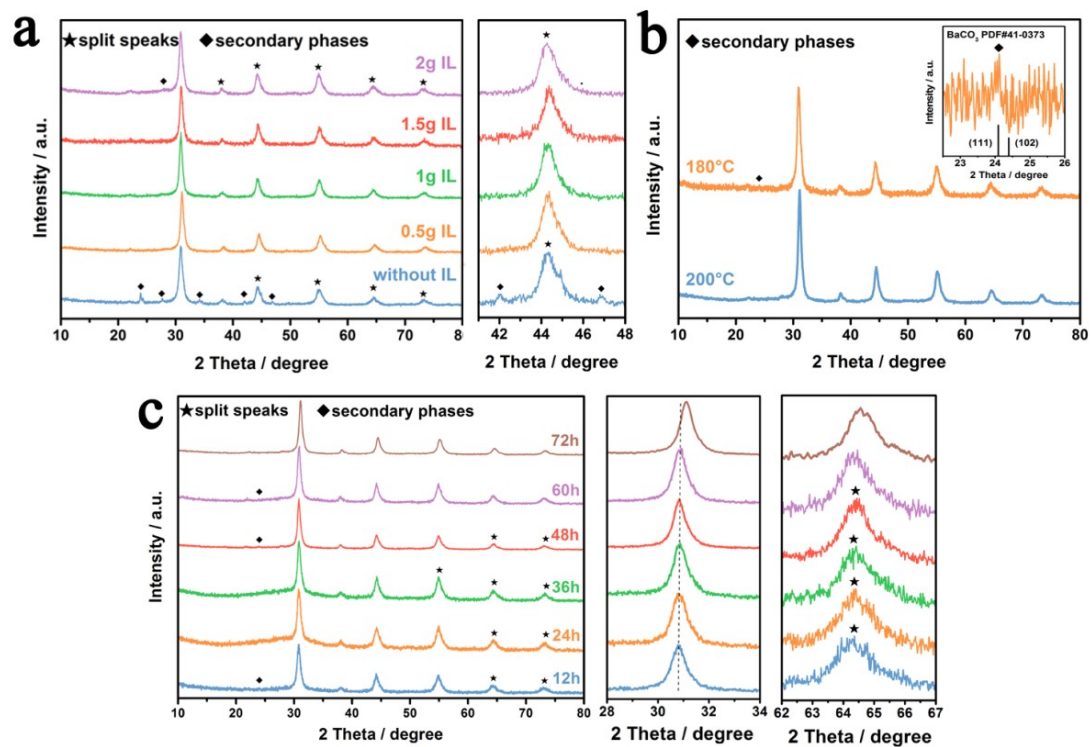
Fig. S12. (a) XRD patterns of Ba(FeTiNbZrTa)O$_3$ with different amount of [BMMIm]Cl, (b) XRD patterns of Ba(FeNbTiZrTa)O$_3$ with different reaction temperature, (c) XRD patterns of Ba(FeTiNbZrTa)O$_3$ with different reaction time.
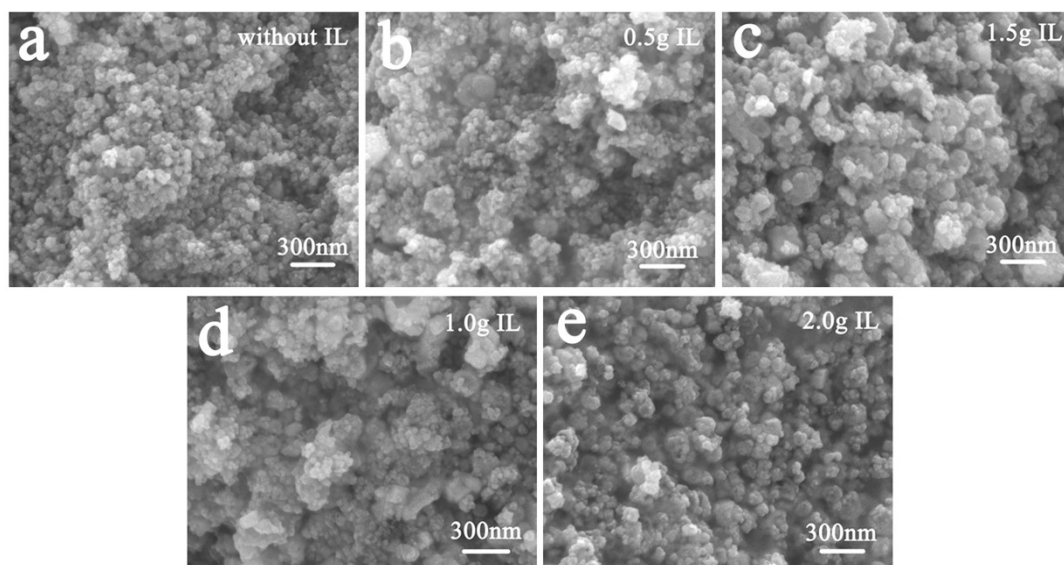
Fig. S13. SEM images of Ba(FeNbTiZrTa)O$_3$ with different amount of [BMMIm]Cl in the synthesis process.
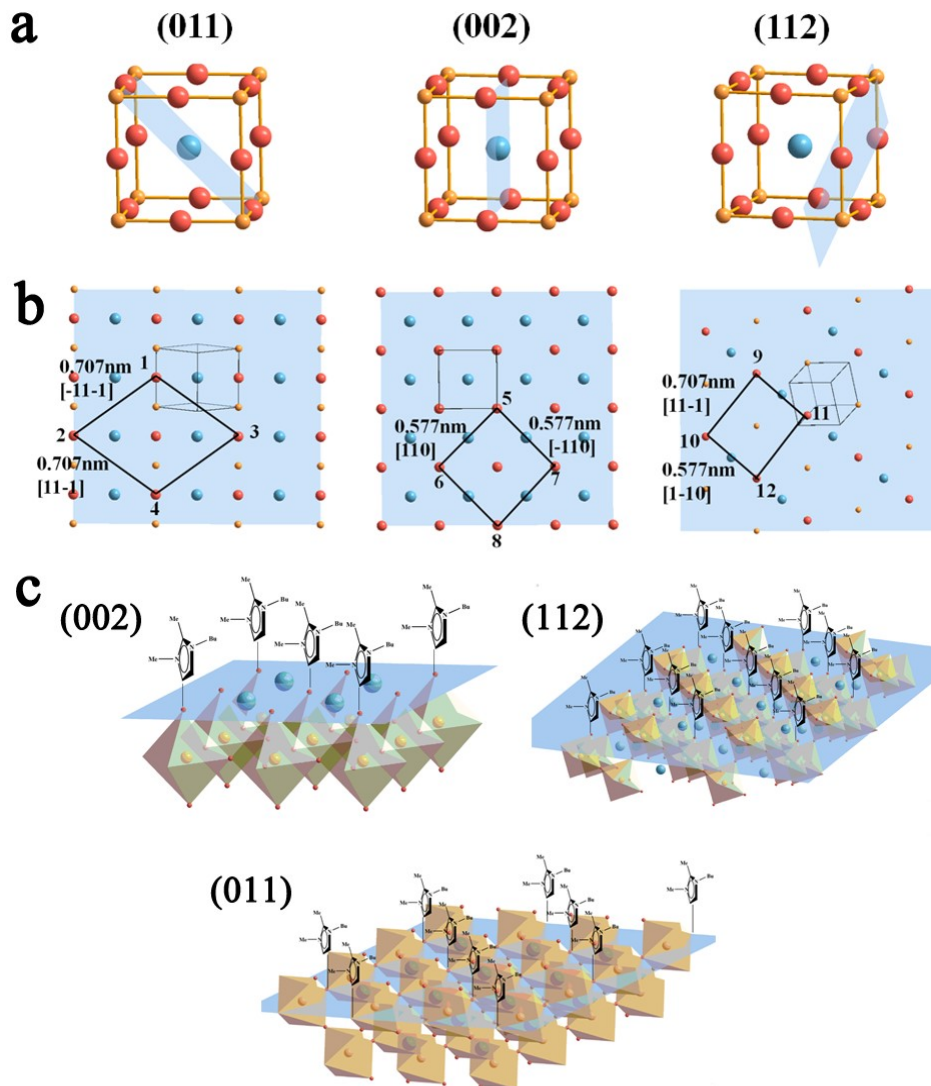
Fig. S14. Schematic illustrations of (a) the (011), (002) and (112) planes of Ba(FeNbTiZrTa)O$_3$, (b) surface structures of the primary stable crystal planes, (c) a projected view of [BMMIm]$^+$ ions anchored onto (011), (002) and (112) planes to form tight coverage layers. Blue atoms: Ba, yellow atoms: B site metals and red atoms: O.

The large viscosity of [BMMIm]Cl-KOH system and the low reaction temperature results in a relatively slow growth of perovskite,[1] which is important for the formation of dispersive and small-sized nanoparticles of Ba(FeNbTiZrTa)O$_3$; meanwhile, [BMMIm]Cl plays another major

role. As the supramolecular fluid, ILs feature multiple coexisting interactions, such as hydrogen bonds, electrostatic interactions and π-π stacking.[2, 3] Because of surface basic properties, positive charged [BMMIm]$^+$ ions can absorb on the surface of Ba(FeNbTiZrTa)O$_3$, so adsorbing competition between K$^+$, Ba^{2+} and [BMMIm]$^+$ is then considered. Although K$^+$ or Ba^{2+} ions present higher electrostatic effect, [BMMIm]$^+$ ions have more preference for adsorbing on the surface of Ba(FeNbTiZrTa)O$_3$. Besides electrostatic interactions, three other factors can be identified for the adsorption of [BMMIm]$^+$ ions: the first factor is the large steric hindrance of [BMMIm]$^+$ ions, which will hinder the diffusion of K$^+$ and Ba^{2+} ions toward the surface of Ba(FeNbTiZrTa)O$_3$; the second one is based on the mutual π-stacking interaction between imidazole rings; and the third influencing factor is the hydrogen-bonding interaction between [BMMIm]$^+$ ions and O atoms. The H-bond donor is the C-H unit within an imidazole cation, which can be a C-H on the aromatic ring, or a C-H from the methylene or methyl groups of the alkyl chains.[3, 4] However, stronger hydrogen-bonding interactions are found with the ring C^4-H and C^5-H (≈2.2 Å) in imidazole rings, while alkyl H-bonds are of medium strength, and bond distances are longer and more variable (≈2.3-2.7 Å) depending on the local conformation of the alkyl chain;[4, 5] further considering the steric effect, hydrogen-bonds exist in the formation of O (Ba(FeNbTiZrTa)O$_3$ surface)-H-C^4 ([BMMIm]$^+$ rings).[6, 7]

On the other hand, the adsorption selectivity of [BMMIm]$^+$ ions on the crystal facets of a substrate should be restricted by the geometric matching principle, which means that the adsorption sites of the substrate should meet the space requirement for interionic stacking of imidazole cations.[8] According to previous reports, mutual π-stacking distance between imidazole rings is about 0.6-0.7 nm. The atomic arrangements of the primary stable crystal planes of (011),

(002) and (112) planes for simulated Ba(FeNbTiZrTa)O$_3$ structure are presented in Fig. S14a-S14b, in which the distances between O atoms on the (011) plane along [11-1] and [-11-1] directions are both 0.707 nm, so that [BMMIm]$^+$ can adsorb on (011) plane along [11-1] and [-11-1] directions. In addition, the atom arrangement of the (002) facet indicates that the distances between O atoms are both 0.577 nm along [110] and [-110] directions, while the distances between O atoms are 0.577 nm and 0.707 nm in the directions of [1-10] and [11-1] for the (112) plane of Ba(FeNbTiZrTa)O$_3$, respectively. Accordingly, (011), (002) and (112) planes are appropriate for the mutual π-stacking distance of imidazole rings, and as such, [BMMIm]$^+$ ions can vertically adsorb on these facets to generate compact adsorption layers. As shown in Fig. S14b, [BMMIm]$^+$ ions are located in the 1, 2, 3, 4 sites in (011) plane, 5, 6, 7, 8 sites in (002) plane and 9, 10, 11, 12 sites in (112) plane, respectively. However, the distances between O atoms of 1-4 sites and 2-3 sites are 0.816 nm and 1.154 nm in (011) plane, respectively, which do not meet the space requirement for interionic stacking of imidazole cations. Similarly, the distances between O atoms of 5-8 sites and 6-7 sites are both 0.816 nm in (002) plane, while the distances between O atoms of 9-12 sites and 10-11 sites are both 0.913 nm in (112) plane. Thus, the adsorption layers of [BMMIm]$^+$ ions is most stable in (002) planes due to the minimum deviation from the mutual π-stacking distance of imidazole rings in different directions; on the contrary, the adsorption layers of [BMMIm]$^+$ ions is most unstable in (011) planes, so [BMMIm]Cl has a greater impact on (002) and (112) planes than (011) plane, which accords with XRD results. The projected views of [BMMIm]$^+$ ions adsorbed onto (011), (002) and (112) facets of Ba(FeNbTiZrTa)O$_3$ to form tight coverage layers are presented in Fig. S14c, thus the growth of Ba(FeNbTiZrTa)O$_3$ are inhibited, resulting in the formation of dispersive, small-sized nanoparticles.
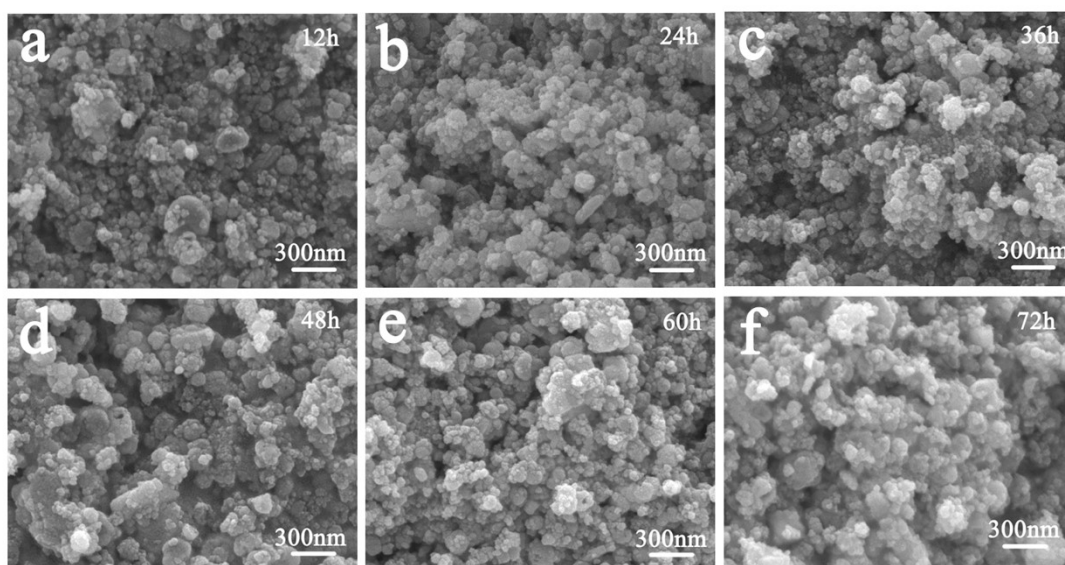
Fig. S15. SEM images of Ba(FeNbTiZrTa)O$_3$ with different reaction time.
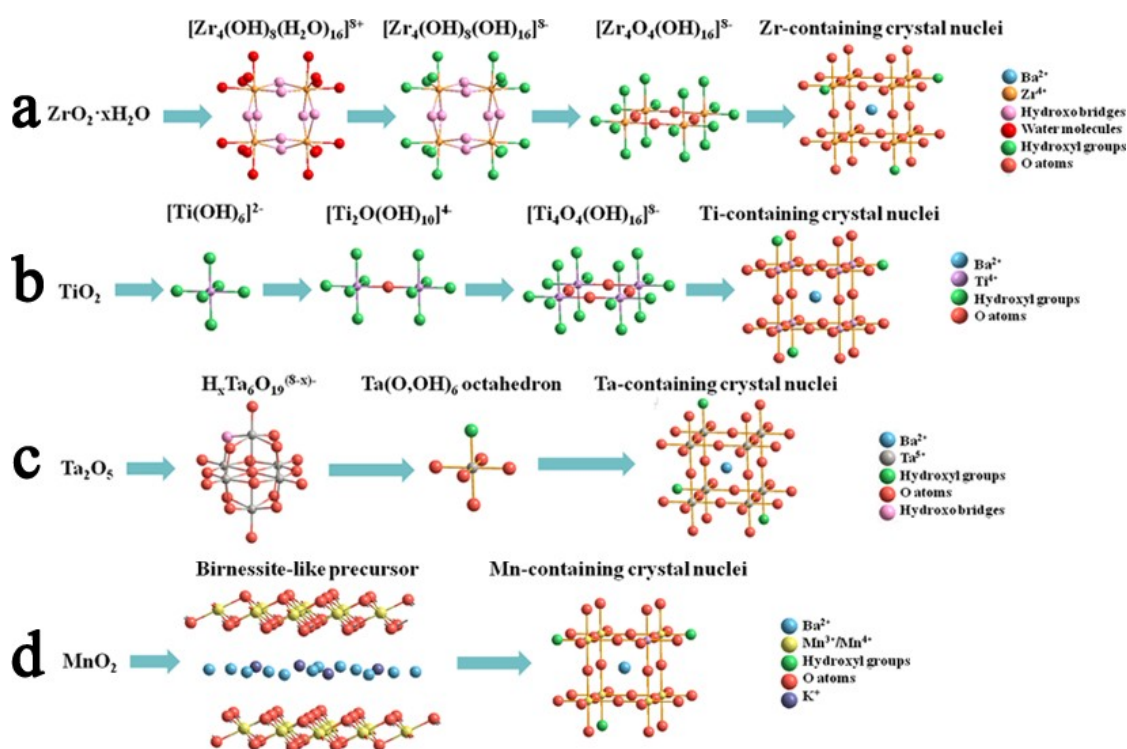
Fig. S16. Schematic representation of the hydrolysis and condensation processes for (a) Zr species, (b) Ti species (Similar process happens to Sn, Fe and V species), (c) Ta species (Similar process happens to Nb species), and (d) Mn species.

At the beginning, ZrOCl$_2$·8H$_2$O is mixed with KOH, resulting in the formation of amorphous ZrO$_2$·xH$_2$O, in which the tetramer complexes with 8 hydroxo bridges and 16 coordinate water molecules, [Zr$_4$(OH)$_8$(H$_2$O)$_{16}$]$^{8+}$, are the major species. Water ligands of tetramer ionize to give the hydroxide complex under basic condition,[9, 10] thus the negative charged tetramer complexes [Zr$_4$(OH)$_8$(OH)$_{16}$]$^{8-}$ are generated. Under proper reaction temperature and basicity, 6-fold Zr species [Zr$_4$O$_4$(OH)$_{16}$]$^{8-}$ linked by bridging O atoms are formed *via* hydrolysis and condensation reactions, which have strong interactions with positive charged barium ions, thus crystal nuclei of perovskite with Zr in B site are formed.

A dissolution-precipitation mechanism is taking place when TiO$_2$ is used as metal source.[11, 12] Ti-O bonds are broken via hydrolytic attack to form hydroxytitanium complexes [Ti(OH)$_x$]$^{4-x}$ capable of dissolution, and the 6-fold Ti coordinated species [Ti(OH)$_6$]$^{2-}$ are the main species at highly basic condition.[13] The subsequent condensation reactions lead to the formation of polymeric chains composed of thermodynamically stable corner-shared Ti(O,OH)$_6$ octahedrons, such as [Ti$_2$O(OH)$_{10}$]$^{4-}$, [Ti$_3$O$_2$(OH)$_{14}$]$^{10-}$, [Ti$_4$O$_4$(OH)$_{16}$]$^{8-}$, in which the skeleton of the polymer corresponds to Ti atoms linked by bridging O atoms.[14] Negative charged polymeric chains of Ti hydroxides react with Ba^{2+} ions, resulting in the formation of crystal nuclei for perovskite with Ti in B site. Similarly, the Sn/Fe-containing crystal nuclei of perovskite are formed from [Sn(OH)$_6$]$^{2-}$ [15, 16] and [Fe(OH)$_6$]$^{3-}$ [17, 18] species, while V-containing crystal nuclei of perovskite are possibly formed from V(OH)$_6{}^{2-}$ species after V(V) is reduced to V(IV).

When MnO$_2$ is used as metal source, a part of Mn(IV) is likely to be reduced to Mn(III) in [BMMIm]Cl-KOH system. The amorphous birnessite-like precursor is formed after

MnO$_2$ is dissolved and partly reduced,[19] which has an octahedral layer structure composed of edge-shared MnO$_6$ octahedron and metal ions located in the interlayer space of the mixed-valent MnO$_6$ octahedron.[20] The birnessite-like precursor is an intermediate phase to crystalline perovskite phase because of the similarity of the Mn-O framework of birnessite and perovskite structures. Subsequently, a dissolution and crystallization process happens to the birnessite-like precursor, and the rearrangement of MnO$_6$ octahedrons occurs, forming thermodynamically stable corner-shared MnO$_6$ structures with Ba^{2+} ions located in the interstitial void of neighboring octahedron, thus Mn-containing crystal nuclei of perovskite are formed.

When Nb$_2$O$_5$ or Ta$_2$O$_5$ is used in the synthesis process, Nb(V) is reduced to Nb(IV), while Ta(V) remains unchanged. Ta$_2$O$_5$ is dissolved into H$_x$Ta$_6$O$_{19}$$^{(8-x)-}$ clusters in [BMMIm]Cl-KOH system, which are composed of six edge-shared Ta(O,OH)$_6$ octahedrons;[21] H$_x$Ta$_6$O$_{19}$$^{(8-x)-}$ clusters will transform to octahedron H$_x$TaO$_6$$^{(7-x)-}$ anions, which act as elementary species for perovskite structures.[22] H$_x$Nb$_6$O$_{19}$$^{(14-x)-}$ is produced and transformed to H$_x$NbO$_6$$^{(8-x)-}$ though similar processes. H$_x$TaO$_6$$^{(7-x)-}$/H$_xNbO_6$$^{(8-x)-}$ anions are linked by bridging O atoms, finally forming thermodynamically stable corner-shared TaO$_6$/NbO$_6$ structures with Ba^{2+} in the interstitial void of neighboring octahedron, thus crystal nuclei of perovskite with Ta/Nb in B site are formed.

Table S1. The element composition of Ba(FeNbTiZrTa)O$_3$ determined by ICP-OES.

Element	Ba	Fe	Nb	Ti	Zr	Ta
Content (wt%)	63.5	6.37	13.7	5.75	10.9	24.4
Atomic ratio	Fe/Nb/Ti/Zr/Ta = 0.179:0.232:0.189:0.188:0.212 A/B (A=Ba, B=Fe, Ti, Nb, Zr, Ta) = 0.727					

Table S2. Content of hydroxyl defects in Ba(FeNbTiZrTa)O$_3$.

Material	Content of hydroxyl defects
Before etching	33.7%
Etch time: 100s	10.6%
Etch time: 200s	11.1%

Table S3. The ratio of diffraction peak intensity between (011), (002) and (112) planes in Ba(FeNbTiZrTa)O$_3$ structure.

IL dosage / g	0	0.5	1	1.5	2
$I_{(002)}$ / $I_{(011)}$	25.7%	27.8%	30.8%	32.7%	34.4%
$I_{(112)}$ / $I_{(011)}$	23.2%	26.1%	28.0%	29.6%	32.1%

Table S4. Stability constants of metal ion-hydroxyl coordination compounds.[23-25]

Metal ion	$logK_1$	$logK_2$	$logK_3$	$logK_4$
Fe (III)	11.87	21.17	29.67	-
Ti (IV)	-	-	11.9	10.3
Zr (IV)	14.3	28.3	41.9	55.3
V (IV)	8.6	-	-	-
V (V)	-	25.2	-	46.2
Sn (IV)	-	-	-	57.3

Table S5. Comparison of different synthesis methods for HEPOs.

Materials	Method	Mental sources	Reaction conditions	Particle size	References
$Ba(FeNbTiZrTa)O_3$, $Ba(MnNbTiZrTa)O_3$, $Ba(FeSnTiZrTa)O_3$, $Ba(FeVTiZrTa)O_3$	Ionic liquid-hydroxide-mediated method	Mental oxides, mental nitrate salts, et al.	Synthesized at 200°C or lower for 72h	20-60nm, mean particle size of 36nm	This paper
$Sr(Zr_{0.2}Sn_{0.2}Ti_{0.2}Hf_{0.2}Mn_{0.2})O_3$, $Sr(Zr_{0.2}Sn_{0.2}Ti_{0.2}Hf_{0.2}Nb_{0.2})O_3$, $Ba(Zr_{0.2}Sn_{0.2}Ti_{0.2}Hf_{0.2}Ce_{0.2})O_3$, $Ba(Zr_{0.2}Sn_{0.2}Ti_{0.2}Hf_{0.2}Y_{0.2})O_{3-x}$, $Ba(Zr_{0.2}Sn_{0.2}Ti_{0.2}Hf_{0.2}Nb_{0.2})O_3$, $(Sr_{0.5}Ba_{0.5})(Zr_{0.2}Sn_{0.2}Ti_{0.2}Hf_{0.2}Nb_{0.2})O_3$	Solid phase sintering method	Mental oxides	High energy ball milled, calcined at 1300-1500°C for 10h.	Not reported	[26]
$(Gd_{0.2}La_{0.2}Nd_{0.2}Sm_{0.2}Y_{0.2})CoO_3$, $La(Co_{0.2}Cr_{0.2}Fe_{0.2}Mn_{0.2}Ni_{0.2})O_3$, $(Gd_{0.2}La_{0.2}Nd_{0.2}Sm_{0.2}Y_{0.2})(Co_{0.2}Cr_{0.2}Fe_{0.2}Mn_{0.2}Ni_{0.2})O_3$, et al.	Nebulised spray pyrolysis method	Mental nitrate salts	Formed at a temperature of 1050°C and a pressure of 900mbar, further calcined at 1200°C for 2h.	50-450nm, mean particle size of 180nm	[27]
$Sr((Zr_{0.94}Y_{0.06})_{0.2}Sn_{0.2}Ti_{0.2}Hf_{0.2}Mn_{0.2})O_{3-x}$	Reactive spark plasma sintering	Mental oxides	Sintered at 1450°C and 1375°C for 9min	Long-range homogeneous microstructure with a few	[28]

				residual pores	
$La_{1-x}Sr_x(CoCrFeMnNi)O_{3-\delta}$	sol-gel method	Mental nitrate salts	Calcined at 700°C for 6h, further calcined at 1000°C for 20h	Not reported	[29]
$(Gd_{0.2}Nd_{0.2}La_{0.2}Sm_{0.2}Y_{0.2})CoO_3$	Coprecipitation hydrothermal method	Mental nitrate salts	Hydrothermal synthesized at 150°C for 72h and calcined at 1200°C for 2h.	A homogenous distribution of few-micrometer-diameter grains	[30]
$Ba(Zr_{0.2}Sn_{0.2}Ti_{0.2}Hf_{0.2}Nb_{0.2})O_3$ thin films	Pulsed laser deposition method	Ceramic target substrate of $Ba(Zr_{0.2}Sn_{0.2}Ti_{0.2}Hf_{0.2}Nb_{0.2})O_3$ synthesized by solid-state reaction method	Oxygen partial pressure of 150mTorr at a substrate temperature of 750°C	Thicknesses of 7, 26 and 72 nm.	[31]
$BaSr(ZrHfTi)O_3$, $BaSrBi(ZrHfTiFe)O_3$	Ultrasonication-based method	Mental chlorides	Room-temperature	Average diameter of (76 ± 1.7)nm	[32]

References

1. H. Liu, C. Hu and Z. L. Wang, Nano Lett., 2006, 6, 1535-1540.

2. Z. Ma, J. Yu and S. Dai, Adv. Mater., 2010, 22, 261-285.

3. Y.-L. Wang, B. Li, S. Sarman, F. Mocci, Z.-Y. Lu, J. Yuan, A. Laaksonen and M. D. Fayer, Chem. Rev., 2020, 120, 5798-5877.

4. P. A. Hunt, C. R. Ashworth and R. P. Matthews, Chem. Soc. Rev., 2015, 44, 1257-1288.

5. P. A. Hunt and I. R. Gould, J. Phys. Chem. A, 2006, 110, 2269-2282.

6. W. Zheng, X. Liu, Z. Yan and L. Zhu, ACS Nano, 2009, 3, 115-122.

7. Y. Liu, Q. Xu, R. Wang, Y. Zheng, Z. Wang and W. Zheng, ACS Appl. Mater. Inter., 2020, 12, 5775-5785.

8. K. Qi, Q. Qin, X. Duan, G. Wang, L. Wu and W. Zheng, Chem.-Eur. J., 2014, 20, 9012-9017.

9. H.-S. Kil, S.-H. Hwag, J.-H. Ryu, D.-Y. Lim and S.-B. Cho, J. Ceram. Soc. Jpn., 2012, 120, 52-57.

10. H. Wang, G. Li, Y. Xue and L. Li, J. Solid State Chem., 2007, 180, 2790-2797.

11. J. O. Eckert, C. C. Hung-Houston, B. L. Gersten, M. M. Lencka and R. E. Riman, J. Am. Ceram. Soc., 2010, 79, 2929-2939.

12. R. I. Walton, F. Millange, R. I. Smith, T. C. Hansen and D. O'Hare, J. Am. Chem. Soc., 2001, 123, 12547-12555.

13. B. N. Ryzhenko, N. I. Kovalenko and N. I. Prisyagina, Geochem. Int., 2006, 44, 879-895.

14. A. Testino, M. T. Buscaglia, V. Buscaglia, M. Viviani, C. Bottino and P. Nanni, Chem. Mater., 2004, 16, 1536-1543.

15. Y. Liu, J. Li and I. M. Chou, Am. Mineral., 2020, 105, 664-673.

16. E. J. Yeom, S. S. Shin, W. S. Yang, S. J. Lee, W. Yin, D. Kim, J. H. Noh, T. K. Ahn and S. I. Seok, J. Mater. Chem. A, 2017, 5, 79-86.

17. Z. Chen, G. Zhan, X. He, H. Yang and H. Wu, Cryst. Res. Technol., 2011, 46, 309-314.

18. B. Li, H.-J. Sun, W. Chen, C.-Y. Zhang, Y.-B. Wang, J. Shen, J. Zhou and X.-F. Liu, Chinese J. Inorg. Chem., 2009, 25, 1848-1852.

19. Y. Chen, H. Yuan, G. Tian, G. Zhang and S. Feng, J. Solid State Chem., 2007, 180, 167-172.

20. X. F. Shen, Y. S. Ding, J. Liu, J. Cai, K. Laubernds, R. P. Zerger, A. Vasiliev, M. Aindow and S. L. Suib, Adv. Mater., 2005, 17, 805-809.

21. M. Nyman, T. M. Alam, F. Bonhomme, M. A. Rodriguez, C. S. Frazer and M. E. Welk, J. Clust. Sci., 2006, 17, 197-219.

22. Y. Hu, H. Gu, Z. Hu, W. Di, Y. Yuan, J. You, W. Cao, Y. Wang and H. L. W. Chan, Cryst. Growth Des., 2008, 8, 832-837.

23. T. Sugimoto, X. Zhou and A. Muramatsu, J. Colloid Interf. Sci., 2002, 252, 339-346.

24. F. Séby, M. Potin-Gautier, E. Giffaut and O. F. X. Donard, Geochim. Cosmochim. Acta, 2001, 65, 3041-3053.

25. J. Dean, Lange's handbook of chemistry /-13th ed, Science Press, Beijing, 1991.

26. S. Jiang, T. Hu, J. Gild, N. Zhou, J. Nie, M. Qin, T. Harrington, K. Vecchio and J. Luo, Scripta Mater., 2018, 142, 116-120.

27. A. Sarkar, R. Djenadic, D. Wang, C. Hein, R. Kautenburger, O. Clemens and H. Hahn, J. Eur. Ceram. Soc., 2018, 38, 2318-2327.

28. M. Biesuz, S. Fu, J. Dong, A. Jiang, D. Ke, Q. Xu, D. Zhu, M. Bortolotti, M. J. Reece, C. Hu and S. Grasso, J. Asian Ceram. Soc., 2019, 7, 127-132.

29. J. Dabrowa, A. Olszewska, A. Falkenstein, C. Schwab, M. Szymczak, M. Zajusz, M. Mozdzierz, A. Mikula, K. Zielinska, K. Berent, T. Czeppe, M. Martin and K. Swierczek, J. Mater. Chem. A, 2020, 8, 24455-24468.

30. P. A. Krawczyk, M. Jurczyszyn, J. Pawlak, W. Salamon, P. Baran, A. Kmita, L. Gondek, M. Sikora, C. Kapusta, T. Straczek, J. Wyrwa and A. Zywczak, ACS Appl. Electron. Mater., 2020, 2, 3211-3220.

31. Y. Sharma, B. L. Musico, X. Gao, C. Hua, A. F. May, A. Herklotz, A. Rastogi, D. Mandrus, J. Yan, H. N. Lee, M. F. Chisholm, V. Keppens and T. Z. Ward, Phys. Rev. Mater., 2018, 2, 060404.

32. F. Okejiri, Z. Zhang, J. Liu, M. Liu, S. Yang and S. Dai, Chemsuschem, 2020, 13, 111-115.